Second harmonic responses of clickable azobenzenes in solution

Dellai, Angela; Courdurié, Chloé; Dubuis, Simon ; Kaka, Komlanvi Sèvi; Champagne, Benoît; Vellutini, Luc ; Genin , Emilie ; Rodriguez, Vincent; Castet, Frédéric

Published in:
Dyes and pigments

DOI:
10.1016/j.dyepig.2023.111744

Publication date:
2023

Document Version
Peer reviewed version

Second Harmonic Responses of Clickable Azobenzenes in Solution: Comparative Hyper-Rayleigh Scattering and Density Functional Theory Studies

Angela Dellai,[1,‡] Chloé Courdurié,[1,‡] Simon Dubuis,[1,‡] Komlanvi Sèvi Kaka,[1,2] Benoît Champagne,[2] Luc Vellutini,[1,*] Emilie Genin,[1,*] Vincent Rodriguez[1,*] and Frédéric Castet[1,*]

[1] Univ. Bordeaux, CNRS, Bordeaux INP, ISM, UMR 5255, F-33405 Cedex Talence, France.
[2] Theoretical Chemistry Laboratory, Unit of Theoretical and Structural Physical Chemistry, NISM (Namur Institute of Structured Matter), University of Namur (UNamur), B-5000 Namur, Belgium.
[‡] AD, CC and SD contributed equally to this work.

Abstract

The linear and second-order nonlinear optical (NLO) properties of clickable azobenzene derivatives are investigated in chloroform solution by means of UV/Visible and Hyper-Rayleigh scattering (HRS) spectroscopies. Their absorption properties are also monitored along time in order to characterize the rate and kinetics of the E-Z photoswitching reaction. The magnitude and symmetry of the first hyperpolarizability of the compounds are rationalized with the help of DFT calculations, which support well the experimental data. We demonstrate that the second harmonic generation (SHG) intensity of the E form, as well as its variation upon photoisomerization, can be tuned by varying the nature of the peripheral substituents. A fully characterized library of ready-to-click switchable compounds displaying large hyperpolarizability contrasts, and differing in the amplitude and orientation in their dipole moments is provided. This library expands the database of photoswitching compounds for further anchorage into polymer matrices or nano- or micro-sized solid substrates.

1 Introduction

Over the last twenty years, the development of click chemistry has opened up broad horizons in materials science,[1] as it is a versatile tool for chemical modification of substrates and fine tuning of their physicochemical properties.[2,3] In this context, azide-terminated Self-Assembled Monolayers (SAMs) are widely used to immobilize (bio)chemical species on solid support by click chemistry.[4,5] Among the wide range of possible applications,[6,7] photoreactive SAMs functionalized with organic photochromes that undergo significant changes in their first hyperpolarizabilities (β) upon isomerization are of great interest for

photonic technologies. Indeed, exploiting the non-resonant character of NLO processes such as second harmonic generation (SHG) enables the development of chemical detection devices or optical memories with non-destructive reading capability.

Since they are the basic building blocks of these materials, the design of molecular NLO switches exhibiting fast and reversible photoconversion together with high β-contrast has motivated a large number of studies.[8,9] Different classes of photochromes meeting the required specifications have been developed during the last three decades, such as spiroheterocyclic compounds (including spiropyrans,[10] spirooxazines,[11] spirocyclohexadines[12] or benzazolo-oxazolidines[13–19]), diarylethene,[20] dithiazolylethene,[21] dihydroazulene[22] and fulgimide[23,24] derivatives, or more recently reverse photochromes such as Donor-Acceptor Stenhouse Adducts (DASAs).[25,26] All these systems involve the cleavage or formation of a chemical bond in their photochromic mechanism, and interconvert between a cyclized (closed) form and an extended (open) one. Due to the wide variation of π-electron conjugation upon photoisomerization, strong hyperpolarizability contrasts have been recorded for some of these systems when asymmetrically functionalized by efficient donor-acceptor end groups. Lower NLO contrasts are usually associated with photochromes based on a tautomeric equilibrium, such as salicylideneanilines.[27–29] However, the small geometric distortion associated with the photoinduced proton migration ensures good efficiency of the switching process in both solution and solid state,[30–33] and therefore a good fatigue resistance to the material.

The efficient and reversible photoisomerization in azobenzenes has also been exploited to prepare switchable NLO materials, as the *trans-cis* reaction is commonly accompanied by a significant change in the second-order NLO response. The decrease of the SHG intensity upon photoisomerization was observed for the first time in electric field-poled thin films of poly(methyl methacrylate) doped with disperse red one (DR1).[34] More recently, reversible switching of the NLO response upon alternative exposure to UV and visible lights was also demonstrated in azobenzene-functionalized SAMs, revealing changes of 16% in the normal SHG intensity.[35,36] As shown in previous computational works,[37–40] chemical modifications of the azobenzene chromophores with appropriate donor/acceptor groups can significantly enhance the first hyperpolarizability of the *trans* form, a strategy that could therefore be used to increase further the SHG contrast of 2D materials based on these photochromes. However, high NLO responses are obtained for highly dipolar systems, and

strong dipole-dipole interactions could affect the spatial organization of the chromophores after their anchorage onto a substrate. The amplitude and orientation of the molecular dipoles should thus be also considered in the optimal substitution pattern of NLO chromophores.

In this work, we report a detailed investigation of the NLO properties of a series of azobenzene derivatives in chloroform solution. Our study combines Hyper-Rayleigh Scattering (HRS) measurements and Density Functional Theory (DFT) calculations, and focuses on the impact of chemical substitution on the magnitude and dipolar/octopolar nature of the second-harmonic signal. The absorption spectra of all derivatives were also recorded in real time in order to monitor the kinetics of the photoswitching process. All derivatives have been designed with a clickable alkyne unit connected in para position to the azobenzene core by using various types of linkers, namely amide (**1** and **2**), ether (**3**) and tertiary amine (**4** and **5**) linkers (by convention located on the left side of the molecules in Figure 1). The phenyl ring on the right-hand side is either non-substituted or functionalized in para with electron-releasing (**NHAc** and **NMe_2**) or electron-withdrawing (**NO_2**) groups. These nine azobenzene derivatives varying by the nature of the linker and the terminal substituent have been synthesized, providing a library of ready-to-click compounds with different amplitudes in their ground state intramolecular charge transfer and SHG response. The impact of clicking a triazole bearing long carbon chain on the alkyne is also investigated in the last part of this study (compounds **L1-4NO_2** and **L2-4NO_2**).

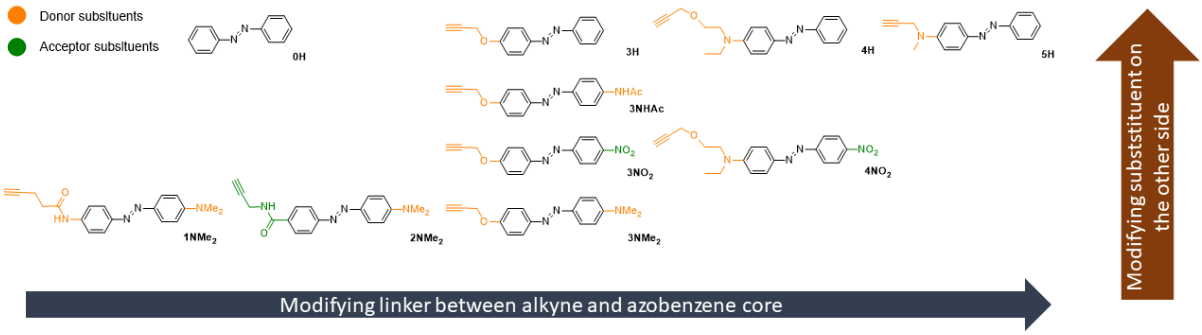

Figure 1: Sketch of the investigated compounds. In addition to the synthesized derivatives, the non-substituted azobenzene (**0H**) has also been considered in the calculations for comparison purposes.

2 Experimental and computational characterizations

2.1 Synthesis and characterization of the dyes

All azobenzene derivatives have been prepared in one or two steps with, for most of them, overall yields higher than 50%. Alkyne terminations have been added through a peptide coupling reaction with the corresponding acid or amine, or through alkylation of the corresponding azobenzene precursors with propargyl bromide (Figure 2). The latter have been either prepared according a classical AZO coupling reaction or bought when commercially available. The details on the synthesis and characterization of all compounds are reported in the Supporting Information, part 1 (SI1).

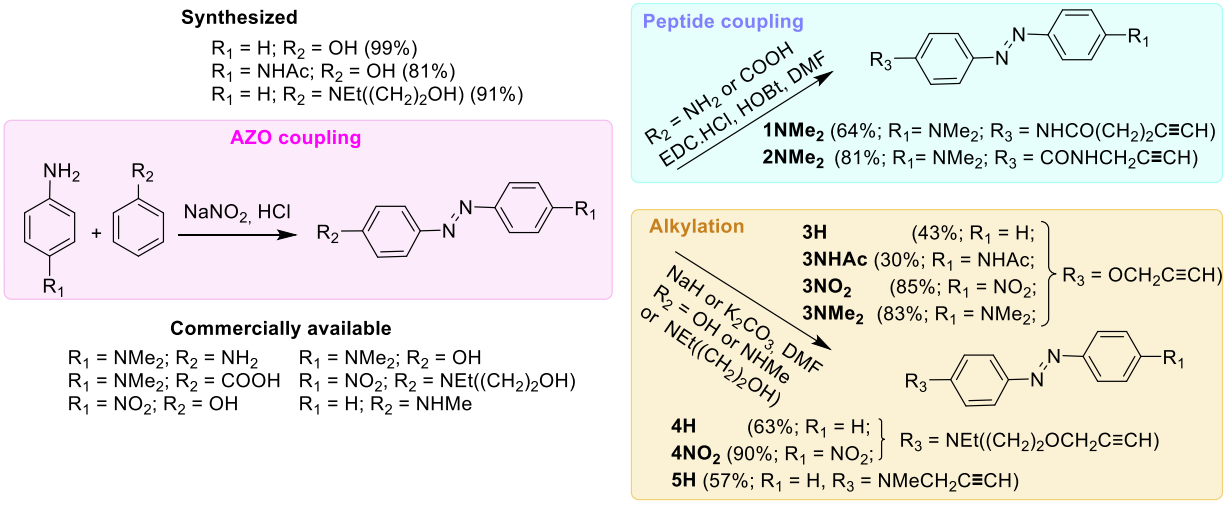

Figure 2: Schematic synthesis pathways leading to the investigated compounds.

2.2 UV-Vis and linear absorption photoswitching kinetics measurements

UV-Vis absorption spectra in the 300-800 nm range were recorded using a Perkin Elmer 650 Lambda spectrometer in diluted chloroform solutions with chromophore concentrations of 5 × 10^{-4} mol/L (±2%). The optical path of the cells was 1 mm.

The *trans-cis* photoswitching was monitored using a recently developed fast acquisition rate spectrometer setup.[26] A broadband light source (tungsten lamp) was used for the spectral monitoring, whose input power was reduced using optical density filters to avoid degradation of the chromophores. Iris diaphragms added on both sides of the sample allowed to adjust the probing beam diameter, (fixed at around 2 mm) and to reduce spurious reflection or scattering. Relative fast changes in absorbance were measured by means of an Ocean Optics USB 2000+

UV−Vis−NIR fiber spectrometer, by averaging two spectra, each at a rate of 1 ms acquisition time. Two light-emitting diodes at 365 nm (λ_{exc}^1) and 405 nm (λ_{exc}^2) (with a rather sharp spectral bandwidth of *ca* 5 nm and with total power density of 3980 and 3650 W/m^2, respectively) were used as excitation sources for the photoswitching from *trans* (E) to *cis* (Z) and maintained at a constant output power (530 mW at 365 nm and 485 mW at 405 nm) for every sample. The excitation beam irradiated a surface of approximately 13 mm of diameter centered on the path of the pump beam. A much larger surface of the pump vs probe beam was preferred in order to minimize/avoid inhomogeneity of the E/Z population in the probed volume during the time acquisitions. Two probe absorbance wavelengths, respectively at 380 nm (λ_{probe}^1) and 420 nm (λ_{probe}^2), were selected in order to characterize and compare the nine compounds that absorb in a broad spectral range (350-550 nm). All experiments were done at room temperature.

The time evolution of the absorbance along the *trans-cis* photoisomerization was fitted with good precision using a first-order exponential law including three fitting parameters A_1, A_2, and τ:

$$\mathrm{A}(t) = A_1 + A_2 e^{-t/\tau} \qquad (1)$$

where $\mathrm{A}(t)$ is the monitored absorbance at λ_{probe}^1 or λ_{probe}^2. $A_2 > 0$ for the *trans*-to-*cis* photoisomerization and $A_2 < 0$ for the back thermal reaction (*cis-to-trans*). τ is the time constant characteristic of the process. τ_{PS} and τ_R are used for the *trans*-to-*cis* and *cis*-to-*trans* processes, respectively. The photoswitching rate ($\%PS$) is assimilated to the absorption contrast and defined as the difference between the absorbances at $t = 0$ and $t \to \infty$ ($A_\mathrm{i} - A_\infty = A_2$), divided by the initial absorbance ($A_\mathrm{i} = A_1 + A_2$):

$$\%PS = 100\left(\frac{A_\mathrm{i} - A_\infty}{A_\mathrm{i}}\right) \qquad (2)$$

According to equation 2, %PS = 100% means that all molecules have switched. The experimental uncertainty on $\%PS$ was estimated to be within 3%, based on the signal-to-noise ratio (SNR) of the spectrometer.

2.3 Hyper-Rayleigh Scattering measurements

HRS measurements were performed using a homemade setup that has been extensively described in previous papers.[15,26] Molecular first hyperpolarizabilities were determined

from the intensity of the incoherent scattered light at the second harmonic frequency of a picosecond laser source at 1064 nm or from the idler signal of a tunable Optical Parametric Generator (OPG) at 1300 nm. We present below the main experimental quantities that are discussed in this study, and refer the reader to Refs. [15,26] for further details on their acquisition. Assuming a polarized incident laser light and observation of a vertically polarized scattered light at 90° (perpendicular to the horizontal plane of polarization), the total HRS hyperpolarizability reads:

$$\beta_{HRS} = \sqrt{\langle \beta_{ZZZ}^2 \rangle + \langle \beta_{ZXX}^2 \rangle} \quad (3)$$

where $\langle \beta_{ZZZ}^2 \rangle$ and $\langle \beta_{ZXX}^2 \rangle$ are macroscopic isotropic averages proportional to the scattered light intensities for vertically and horizontally plane-polarized incident beams, respectively oriented parallel to the Z and X axes of the laboratory frame. The full expressions of $\langle \beta_{ZZZ}^2 \rangle$ and $\langle \beta_{ZXX}^2 \rangle$ in terms of molecular β-tensor components can be found in Ref. [11]. Their quotient

$$DR = \langle \beta_{ZZZ}^2 \rangle / \langle \beta_{ZXX}^2 \rangle \quad (4)$$

is referred to as the depolarization ratio, and provides information on the dipolar/octupolar symmetry of the second-order NLO response. A limiting DR value of 3/2 or 9 stands for pure octupolar or dipolar responses, respectively. In contrast, a prototype push-pull π-conjugated molecule, for which the β tensor is largely dominated by the diagonal component parallel to the molecular charge transfer axis, displays a DR value close to 5. All β values reported in this work are given in atomic units (1 a.u. of β = 3.6213 m^4 V^{-1} = 3.2063 × 10^{-53} C^3 m^3 J^{-2} = 8.641 × 10^{-33} esu) according to the T convention of Ref. [41] The experiments were done in diluted chloroform solutions with concentrations ranging from 1×10^{-5} to 5×10^{-4} mol/L. An amorphous quartz cuvette (3x3 mm^2 section) with 3 mm of optical path for the incident laser, and *ca.* 1.5 mm of optical path was used for the HRS measurements.

2.3 Quantum chemical calculations

Equilibrium geometries of *trans* (E) and *cis* (Z) isomers have been optimized using Density Functional Theory (DFT) with the long-range corrected (LRC) ωB97X-D[42] exchange-correlation functional (XCF) together with the 6-311G(d) basis set. The ωB97X-D XCF, which includes respectively 22% and 100% of Hartree-Fock (HF) nonlocal exchange at short and long-range (with a range separation parameter of 0.2 $Bohr^{-1}$), was identified as a good compromise for geometry optimization of azobenzenes after benchmark calculations using second-order

Møller-Plesset (MP2) results as reference (see the Supporting Information part 3, SI3). Moreover, it was shown that London dispersion corrections are necessary to accurately describe the relative energies between E and Z isomers.[43,44] Optimized geometries were confirmed to be real minima by harmonic frequency calculations. Vertical absorption properties and second-order NLO responses were computed at the M06-2X/6-311+G(d) level. Several previous works proved this level of approximation reliable for calculating the first hyperpolarizabilities of push–pull conjugated dyes, owing to the substantial amount (54%) of long-range Hartree–Fock exchange included in the M06-2X functional[45] and the good balance of the 6-311+G(d) basis set, which includes both polarization and diffuse functions for all non-hydrogen atoms.[46,47] The suitability of M06-2X for computing the first hyperpolarizability of azobenzene derivatives was further evaluated here against other types of XCFs (SI3). Solvent effects (chloroform) were included in all calculations by means of the integral equation formalism of the polarized continuum model (IEF-PCM).[48] Optical properties were computed by using the non-equilibrium limit of IEF-PCM. The static dielectric constant of chloroform, ϵ_0, is equal to 4.71 while the optical one, ϵ_∞, reduces to 2.09. Note that static first hyperpolarizabilities were computed using both ϵ_0 and ϵ_∞; this last scheme was used to ensure continuity of the evolution of dynamic β values with incident wavelength in the $\lambda \to \infty$ limit.

3 Results and discussion

3.1 Structural and ground-state electronic properties

Table 1 reports the Gibbs free energies of the E→Z reaction. As expected, the *trans* isomer is the most thermodynamically stable for all derivatives. Note that **1NMe$_2$**, **2NMe$_2$** and **3NHAc** have each two rotamers with slightly different Gibbs energies. They were considered in the calculations of the optical properties by weighting their respective responses by their statistical population according to a Maxwell-Boltzmann analysis (see Table S9, SI3). All other investigated compounds possess only one structure populated at room temperature.

In all *trans* derivatives, the azobenzene core is fully planar, and the right-hand side group lies in the azobenzene plane. Left-hand side groups that incorporate ether (**3**) and N-alkyl (**4** and **5**) linkers have also a planar backbone, as well as the NHCO amide linker in **1NMe$_2$**. Reversely, the CONH amide group in **2NMe$_2$** shows a deviation from planarity of about 30° due to steric hindrance between the phenyl and amide hydrogens. As a geometrical descriptor of the π-

electron conjugation within the molecules, the bond length alternation (BLA) along the azo-bridge is also reported in Table 1 for *Z* and *E* isomers (see also Table S10 (SI3) and Figure S3 (SI3) for the definition of BLA). As expected, BLA increases upon E→Z isomerization due to the lower π-electron conjugation in the *cis* forms. In both *Z* and *E* isomers, the largest BLA is obtained for the unsubstituted species (**0H**), and it decreases upon functionalization with donor and acceptor units, consistent with the enhancement of the zwitterionic character of the molecular electronic structure. In *trans* isomers, the BLA decreases when increasing the strength of the donor/acceptor substituents, the minimal values being obtained for the push-pull systems **2NMe$_2$**, **3NO$_2$** and **4NO$_2$**. Note that, as reported in an earlier work,[40] the push-pull character of *trans* azobenzene can also be characterized by the ratio Q(π*/π) of the electron occupations of the antibonding π* and bonding π orbitals of the partial N=N double bond, as calculated using Natural Bond Orbital (NBO) population analyses. For compounds investigated here, Q(π*/π) shows a very good correlation with both the azo bond lengths and BLA values (Figure S4, SI3).

All azobenzene derivatives except the non-substituted one (**0H**) have a sizable dipole moment in both their *Z* and *E* isomers (see Table 1), whose amplitude and directionality strongly depend on the chemical functionalization. Push-pull derivatives incorporating both electron-releasing (D) and electron-withdrawing (A) moieties show a decrease of the dipole moment along the trans→cis reaction, as a result of the change in the spatial orientation of the D and A substituents and of the decrease of π-electron conjugation. Reversely, the dipole moment increases upon isomerization for derivatives incorporating two donor units or having only one functionalized phenyl. The change in directionality of the dipole moment with the substitution pattern is illustrated in Figure 2 for representative *E* isomers, together with the electrostatic potential, which pictures the electronic distribution around the molecular skeleton (see Figure S5, SI3 for the other *trans* isomers and Figure S7 for *cis* isomers). The potential maps of **3NO$_2$** and **4NO$_2$** highlight the high electron density located on the nitro group. In such systems having a strong push-pull character, the dipole moment is oriented parallel to the π-conjugation pathway. Replacing the nitro by a dimethyl-amino group (from **3NO$_2$** to **3NMe$_2$**) enriches the electronic density on the azobenzene core, especially around the nitrogen double bond (as also indicated by the large BLA value computed for this compound, see Table 1), and reverts the direction of the dipole vector. In **3NHAc**, the weak donor groups on both sides of the azobenzene core compensate each other, and the direction of the dipole vector is fully

determined by the orientation of the amide group. To further illustrate the impact of chemical functionalization on the electron density distribution, the electrostatic potential-fitted (ESP) atomic charges within the different parts of the compounds are reported in Table S11 (SI3). The asymmetry of the electronic density is reflected in the Δ_{ESP} parameter, defined as the difference in the ESP charge of the two peripheral functionalized phenyls. Expectedly, the largest Δ_{ESP} values (>0.1|e|) are obtained for push-pull systems (**2NMe₂**, **3NO₂** and **4NO₂**), while Δ_{ESP} is close to zero for **3NHAc**, in correlation with the longitudinal component of the molecular dipole moment (Figure S6, SI3). As mentioned in the introduction, the amplitude and orientation of the molecular dipoles may have crucial importance for the subsequent anchorage of the compounds onto a solid substrate, since dipole-dipole interactions impact the spatial organization of the chromophores on the surface. By varying the substitution pattern, clickable compounds have thus been designed with dipoles pointing toward or away from the surface, or parallel to the surface.

Table 1: Relative Gibbs Free Energy ($\Delta G^0_{EZ} = G^0_Z - G^0_E$, kcal/mol) between the *E* (*trans*) and *Z* (*cis*) conformers computed at T = 298.15 K and p = 1 atm at the ωB97X-D/6-311G(d) level in chloroform, bond length alternation (BLA, Å) along the central azo bridge ($BLA = (d_{CN} + d_{NC})/2 - d_{NN}$), and magnitude of the dipole moment of the two forms (μ_E and μ_Z, D).

Compound	ΔG^0_{EZ}	BLA_E	BLA_Z	μ_E	μ_Z
0H	11.64	0.180	0.198	0.00	4.10
1NMe₂	13.74	0.165	0.188	5.58	8.43
2NMe₂	12.29	0.163	0.188	8.38	5.19
3NMe₂	13.19	0.176	0.196	4.43	7.82
3H	13.02	0.171	0.194	1.66	5.03
3NHAc	12.83	0.172	0.193	3.75	7.32
3NO₂	12.23	0.165	0.189	7.55	4.15
4H	12.15	0.168	0.190	2.57	6.52
4NO₂	11.77	0.159	0.181	9.73	7.00
5H	12.75	0.170	0.191	3.57	6.27
L1-4NO₂	13.27	0.159	0.182	14.27	9.70
L2-4NO₂	13.76	0.159	0.182	13.76	9.31

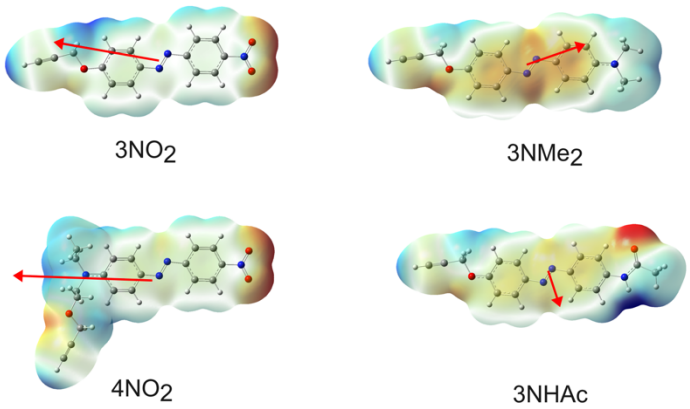

Figure 2: Electrostatic potential maps (with positive (negative) values in blue (red) ranging from –5 10^2 to +5 10^2 a.u.) and dipole moment vectors, as computed at the ωB97X-D/6-311G(d) level in chloroform.

3.2 Absorption properties

The maximal absorption wavelengths and molar extinction coefficients of *E* isomers measured in chloroform are listed in Table 2, while computed spectroscopic data are collected in Table 3 for both *E* and *Z* forms. The experimental and calculated UV-vis spectra are provided in Figures 3 and S11 (SI3). As it is well known for *trans* azobenzenes,[49] the lowest energy band ($S_0 \rightarrow S_1$) is located in the visible range and corresponds to a dipole-forbidden n-π* transition dominated by HOMO-1→LUMO electronic excitations (except **1NMe₂** and **3NMe₂**, for which the n-π* transition involves a HOMO-2→LUMO electron promotion). The shapes of the frontier MOs of *trans* and *cis* isomers are reported in Figure S8-S10 (SI3). The dipole-allowed $S_0 \rightarrow S_2$ transition falls in the UV region and is described by a pure HOMO to LUMO excitation with a π-π* character. Compared to the non-substituted compound (**0H**), chemical functionalization induces a bathochromic shift of the main absorption band, consistent with the decrease of the BLA along the azo bridge. However, the global absorption profile and the nature of the electronic transitions do not change.

As shown in Figure S13 (SI3), the excitation energies towards the first dipole-allowed excited state (S_2) calculated for *trans* isomers at the M06-2X level show an excellent correlation with experimental ones, although they are systematically overestimated. Additional calculations reported on the same plot and carried out using the M06 XCF that contains a lower amount of nonlocal Hartree-Fock exchange (27%) reversely provides underestimated absorption wavelengths.

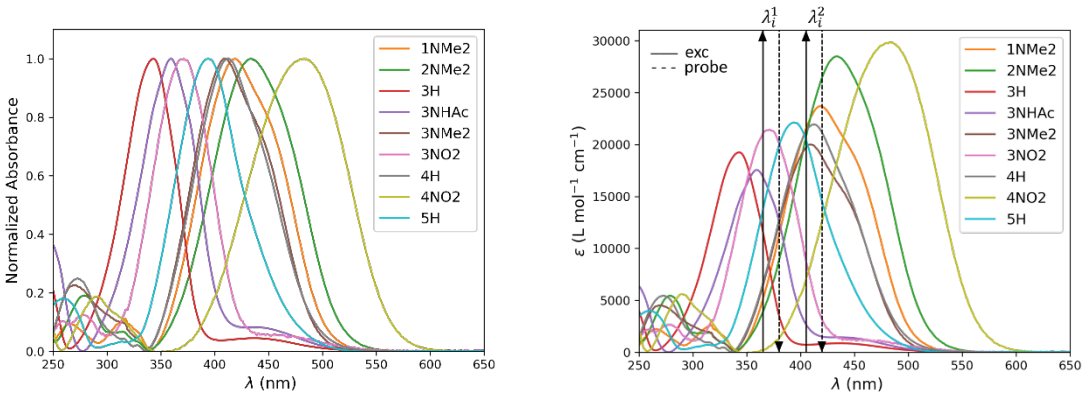

Figure 3: Left: normalized absorbance of *trans* isomers in chloroform solutions. Right: absorption spectra, with λ_i^1 and λ_i^2 wavelengths (*i* = excitation in continuous line and probe in dashed line) used for the photoswitching kinetics (see text).

Table 2: Maximum absorption wavelength (λ_{max}, nm), Full Width at Half Maximum (FWHM, cm^{-1}) and molar extinction coefficient (ϵ_{max} and ϵ_{532}, 10^3 L mol^{-1} cm^{-1}) at λ_{max} and 532 nm of *trans* isomers measured in chloroform.

Compound	λ_{max}	ϵ_{max}	ϵ_{532}	FWHM
1NMe$_2$	419	23.70 ± 1.15	0.20 ± 0.08	5270
2NMe$_2$	434	28.50 ± 0.20	0.90 ± 0.05	4960
3NMe$_2$	410	20.00 ± 1.12	0.10 ± 0.03	5310
3H	343	19.30 ± 0.13	0.00	5260
3NHAc	359	17.60 ± 0.64	0.10 ± 0.07	5190
3NO$_2$	371	21.40 ± 0.35	0.20 ± 0.20	5430
4H	412	21.90 ± 1.48	0.10 ± 0.05	4760
4NO$_2$	483	29.90 ± 2.90	14.20 ± 1.44	4750
5H	394	22.10 ± 0.95	0.10 ± 0.02	4890
L1-4NO$_2$	484	26.00 ± 0.40	13.30 ± 0.18	4710
L2-4NO$_2$	484	29.60 ± 0.55	15.10 ± 0.27	4680

Table 3: Vertical excitation energy (ΔE_{0i}, eV), wavelength (λ_{0i}, nm) and oscillator strength (f_{0i}, dimensionless) of the lowest-energy electronic transitions of *trans* and *cis* isomers, as computed at the TDDFT/M06-2X/6-311+G(d) level in chloroform.

		trans			***cis***		
compound	**transition**	**ΔE_{0i}**	**λ_{0i}**	**f_{0i}**	**ΔE_{0i}**	**λ_{0i}**	**f_{0i}**
0H	$S_0 \rightarrow S_1$	2.54	488	0.000	2.57	482	0.018
	$S_0 \rightarrow S_2$	4.01	309	0.931	4.69	264	0.216

1NMe$_2$	$S_0 \rightarrow S_1$	2.69	461	0.002	2.51	494	0.067
	$S_0 \rightarrow S_2$	3.25	382	1.403	3.85	322	0.449
2NMe$_2$	$S_0 \rightarrow S_1$	2.62	473	0.001	2.54	488	0.065
	$S_0 \rightarrow S_2$	3.21	386	1.303	3.76	330	0.481
3NMe$_2$	$S_0 \rightarrow S_1$	2.71	458	0.000	2.52	492	0.059
	$S_0 \rightarrow S_2$	3.30	376	1.266	3.89	319	0.419
3H	$S_0 \rightarrow S_1$	2.59	479	0.000	2.56	484	0.025
	$S_0 \rightarrow S_2$	3.79	327	1.057	4.41	281	0.285
3NHAc	$S_0 \rightarrow S_1$	2.63	471	0.000	2.53	490	0.037
	$S_0 \rightarrow S_2$	3.59	345	1.331	4.27	290	0.404
3NO$_2$	$S_0 \rightarrow S_1$	2.50	496	0.000	2.54	488	0.037
	$S_0 \rightarrow S_2$	3.53	351	1.210	3.98	312	0.003
	$S_0 \rightarrow S_3$	-	-	-	4.03	308	0.290
4H	$S_0 \rightarrow S_1$	2.65	468	0.000	2.55	486	0.047
	$S_0 \rightarrow S_2$	3.36	369	1.171	3.93	316	0.472
4NO$_2$	$S_0 \rightarrow S_1$	2.56	484	0.000	2.52	492	0.079
	$S_0 \rightarrow S_2$	3.01	412	1.313	3.52	352	0.311
5H	$S_0 \rightarrow S_1$	2.64	470	0.000	2.54	488	0.044
	$S_0 \rightarrow S_2$	3.46	358	1.140	4.01	309	0.446
L1-4NO$_2$	$S_0 \rightarrow S_1$	2.56	484	0.000	2.52	491	0.078
	$S_0 \rightarrow S_2$	3.00	413	1.322	3.52	352	0.304
L2-4NO$_2$	$S_0 \rightarrow S_1$	2.56	484	0.000	2.52	491	0.078
	$S_0 \rightarrow S_2$	3.00	413	1.322	3.52	352	0.306

To gain further insight on the intramolecular charge transfer occurring upon the excitation process in *trans* isomers, Figure 4 illustrates the redistribution of the total electron density induced by the $S_0 \rightarrow S_2$ optical transition for representative *trans* forms (see Figure S13 for the other compounds and *cis* forms). The change in dipole moment upon light excitation ($\Delta\mu_{02}$), as well as the amount of charge transferred (Δq_{02}) and charge transfer distance (Δr_{02}) computed using the procedure proposed by Le Bahers et al.[50],[51] are reported in Table 4. Not surprisingly, push-pull compounds bearing strong donor and acceptor groups at both ends of the azobenzene core display large dipole moment variations upon optical excitation. Consistent with the largest red-shifted absorption band measured for this derivative, the largest $\Delta\mu_{02}$ value (13.7 D) is obtained for **4NO$_2$**, mainly due to a larger charge transfer distance (4.28 Å). On the other hand, the **3NHAc** derivative that incorporates two donor substituents exhibits weak dipole moment variation (0.7 D) and charge transfer distance (0.27 Å), as a result of the opposite light-induced charge transfers from the extremities to the central azobenzene core.

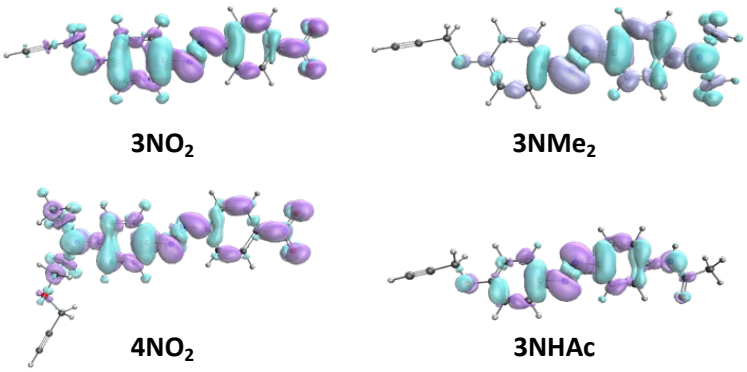

Figure 4: Electron density differences between the S_0 and S_2 electronic states for representative *trans* forms, as calculated at the M06-2X/6-311+G(d) level in chloroform and plotted with isovalues of 0.001. Blue (violet) lobes are associated with negative (positive) values and refer to zones with decreasing (increasing) electron density.

Table 4: Characteristics of the $S_0 \rightarrow S_2$ transition in *trans* isomers, as calculated at the TDDFT/M06-2X/6-311+G(d) level in chloroform: changes in dipole moment ($\Delta\mu_{02} = \|\vec{\mu}_2 - \vec{\mu}_0\|$, D), charge transfers ($\Delta q_{02}$, |e|), and charge transfer distances (Δr_{02}, Å).

Compound	$\Delta\mu_{02}$	Δq_{02}	Δr_{02}
0H	0.000	0.477	0.000
1NMe$_2$	6.280	0.563	2.324
2NMe$_2$	9.686	0.599	3.367
3NMe$_2$	6.195	0.559	2.309
3H	3.776	0.512	1.535
3NHAc	0.523	0.519	0.210
3NO$_2$	9.951	0.591	3.505
4H	8.298	0.605	2.854
4NO$_2$	13.686	0.666	4.276
5H	7.600	0.586	2.700
L1-4NO$_2$	13.780	0.671	4.275
L2-4NO$_2$	13.686	0.673	4.233

Upon *trans-cis* photoisomerization, the intensity of the π→π* band ($S_0 \rightarrow S_2$) decreases, while the n→π* band ($S_0 \rightarrow S_1$) located in the visible range (482-494 nm) becomes slightly allowed (Table 3 and Figures S11-S12, SI3). The spectra computed for *cis* isomers notably differ in the intensity of the $S_0 \rightarrow S_1$ band (formed by a combination of HOMO-1 to LUMO and HOMO to LUMO electron excitations), with oscillator strengths varying from 0.018 (**0H**) to 0.079 (**4NO$_2$**).

3.3 Photoswitching kinetics

In order to characterize the kinetics of the *trans-cis* photoisomerization and back thermal *cis-trans* reaction, the time evolution of the absorption spectrum of each compound was recorded during and after irradiation. As a representative example, the *trans-cis* and *cis-trans* photoswitching behaviors of **2NMe$_2$** are reported in Figure 5, and analyzed using the mono-exponential absorbance fitting described above. The photoswitching kinetics curves for the other systems are provided in SI2. The kinetics data, namely the photoswitching rates (%PS) and characteristic time constants associated to the *trans-cis* and *cis-trans* processes (τ_{PS} and τ_R, respectively), are collected in Table 5. Note that comparison with data reported previously should be made with caution because of the different experimental set-up used.[52,53]

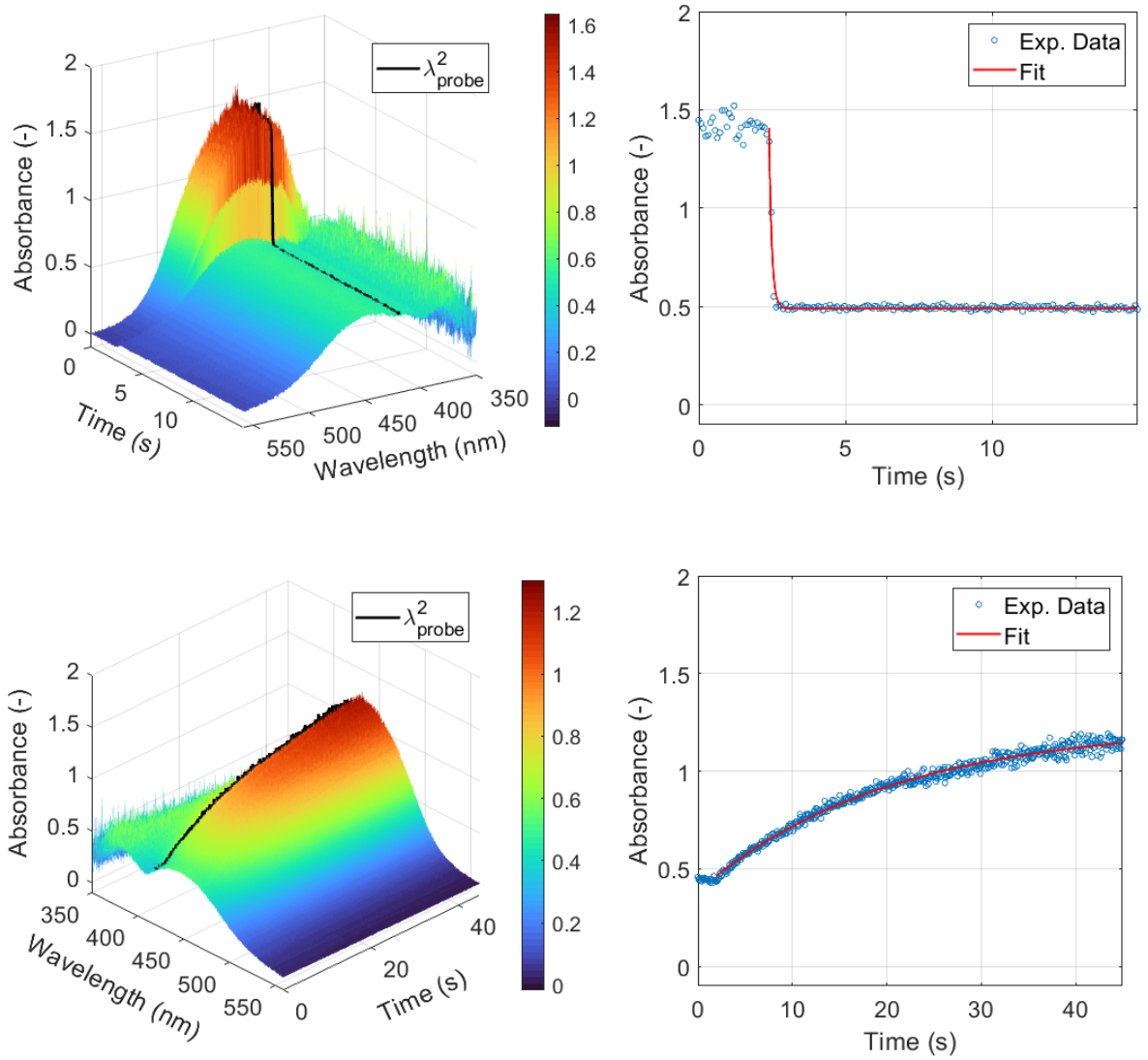

Figure 5: *Trans-cis* (top) and *cis-trans* (bottom) photoisomerization of **2NMe$_2$** monitored at λ^2_{probe} (420 nm) (using λ^2_{exc} for the photoswitching from *trans* to *cis*), and for a concentration

of 4.98 x 10^{-4} mol L^{-1}. The blue dots on the right panels represent the absorbance measured at λ^2_{probe} illustrated by the black line on the left panels. Red lines are exponential fits according equation 1.

The investigated derivatives can be divided in two groups: i) those with maximum absorption wavelength below 400 nm (**3H**, **3NHAc**, **$3NO_2$** and **5H**) which efficiently switch from *trans* to *cis* but do not thermally switch back (grey shading in Table 5), and ii) those with maximum absorbance wavelength above 400 nm (**$1NMe_2$**, **$2NMe_2$**, **$3NMe_2$**, **4H**, **$4NO_2$**), which photoswitch from *trans* to *cis* and thermally switch back to the *trans* form. However, calculations of potential energy profiles and trans-cis isomerization barriers failed to rationalize this different behavior (see SI3).

Table 5: Photoswitching ratios (%PS), and characteristic time constants associated to the *trans*-to-*cis* (τ_{PS}, s) and *cis*-to-*trans* (τ_R, s) processes in chloroform at 5 × 10^{-4} mol/L (±2%).

	Excitation at λ^1_{exc} (365 nm)					
	Monitoring at λ^1_{probe} (380 nm)			**Monitoring at λ^2_{probe} (420 nm)**		
	τ_{PS}	τ_R	**%PS**	τ_{PS}	τ_R	**%PS**
$1NMe_2$	-	-	0	0.08	6.5	32
$2NMe_2$	0.23	0.2	27	0.15	9.2	16
3H	0.08	-	98	-0.19	-	-
3NHAc	0.04	-	98	0.06	-	63
$3NO_2$	0.20	-	68	0.12	-	51
$3NMe_2$	0.19	2.9	29	0.04	2.0	43
4H	-	-	0	0.12	1.8	26
$4NO_2$	-	-	0	-	-	0
5H	0.21	-	54	0.05	-	52

	Excitation at λ^2_{exc} (405 nm)					
	Monitoring at λ^1_{probe} (380 nm)			**Monitoring at λ^2_{probe} (420 nm)**		
	τ_{PS}	τ_R	**%PS**	τ_{PS}	τ_R	**%PS**
$1NMe_2$	0.14	-	39	0.03	56.9	84
$2NMe_2$	-0.41	-	-	0.09	20.1	67
3H	-	-	0	0.08	-	87
3NHAc	0.09	-	61	0.05	-	79
$3NO_2$	0.13	-	53	0.09	-	52
$3NMe_2$	0.06	106.2	52	0.05	113	87
4H	0.26	32.0	25	0.03	198.2	79
$4NO_2$	-0.29	2.9	-	0.08	2.9	22
5H	0.10	-	69	0.03	-	94

For **3NHAc**, **3NO₂** and **5H**, both excitation wavelengths induce efficient *trans*-to-*cis* process, as shown by the photoswitching ratios (%PS > 50%), in accordance with the position of their π-π* bands (Figure 3). **3H**, which presents maximum absorption at the shortest wavelength in the series (343 nm), shows a specific behavior with irradiation at 365 nm. The monitoring at 380 nm is quite fast with τ_{PS} = +0.08 s while for the monitoring at 420 nm, the absorbance increases during irradiation, hence involving a negative τ_{PS} = -0.19 s. We may ascribe this anomalous behavior to the overlap of the *trans* and *cis* bands at 420 nm: according to the calculated values given in Table 3 (see also Figure S12, SI3), the S_0-S_1 *cis* band is expected to occur at *ca* 484 nm, i.e. close to the monitoring wavelength. This effect observed at 420 nm suggests that the dominant absorption band is the *cis* one.

As expected, other derivatives (**1NMe₂**, **2NMe₂**, **3NMe₂**, **4H**, **4NO₂**), with red-shifted π-π* bands above 400 nm, have a less efficient (or no) photoswitching at 365 nm, in contrast with the excitation at 405 nm. For example, **4NO₂** does not switch upon irradiation at 365 nm because it does not absorb at this wavelength. Upon irradiation at 405 nm and monitoring at 380 nm, both **4NO₂** and **2NMe₂** show an anomalous behavior, with a similar increase of the absorbances (negative τ_{PS}) as was observed for **3H** (*vide supra*). Again, an explanation to this behavior could be related to the overlap of the *trans* and *cis* bands at 380 nm. TDDFT calculations give credit to this assumption: according to results in Table 3 and Figure S12 (SI3), the S_0-S_2 *cis* band is expected to occur around 352 nm for **4NO₂** and 330 nm for **2NMe₂**, close to the monitoring wavelength. After correcting the computed absorption wavelengths of *trans* forms (484 nm for **4NO₂** and 330 nm for **2NMe₂**) by using the linear regression of Figure S13 (SI3), one obtains 415 nm for **4NO₂** and 409 nm for **2NMe₂**, which is also close to 380 nm.

Focusing on the results with excitation at 405 nm and monitoring at 420 nm (Table 5), five compounds (**1NMe₂**, **2NMe₂**, **3NMe₂**, **4H**, **4NO₂**) show a very fast (below 1s) *trans*-to-*cis* photoswitching, τ_{PS} ranging between 0.03 to 0.09 s. Apart from **4NO₂**, the *trans*-*cis* isomerization processes are highly efficient, with %PS ranging from 67% (**2NMe₂**) up to 87% (**3NMe₂**). In contrast, their thermal back reactions are among the slowest with τ_R spreading well above 1s, from 2.9 (**4NO₂**) to 198.2 s (**4H**), the shortest time constant corresponding to the strongest push-pull compound in the series (**4NO₂**).

3.4 Nonlinear optical properties

3.4.1 *Experimental and computational NLO responses*

HRS hyperpolarizabilities (β_{HRS}) and depolarization ratios (DR) measured at 1064 and 1300 nm in chloroform are reported in Table 6 for all E isomers. The evolution of the second harmonic light intensity with the incident power and concentration are reported in SI2, as well as its evolution as a function of the incident light polarization. Dipolar and octupolar contributions to the HRS hyperpolarizability according to the irreducible spherical representation of the β tensor are also provided.

As shown in Table 6, the β_{HRS} values measured at 1064 nm are larger than those measured at 1300 nm, owing to dispersion effects. However, at 1064 nm for **4NO₂**, we observed two-photon absorption (TPA), the harmonic response at 532 nm being close to the maximum absorption around 483 nm. Shifting the excitation wavelength from 1064 to 1300 nm allowed us to get rid of TPA and measure undisturbed HRS responses. As expected, the largest β_{HRS} response (17600 a.u.) is obtained at 1300 nm for the strong push-pull derivative (D-π-A type) **4NO₂**. The β_{HRS} at 1300 nm of **2NMe₂**, characterized by a weak acceptor and a strong donor (a-π-D), is well below with β_{HRS} = 7400 a.u. In contrast, the β_{HRS} at 1300 nm of **3NO₂**, characterized by a weak donor and a strong acceptor (d-π-A type), could not be measured due to a weaker NLO response. Considering the dispersion effects, this result is consistent with the β_{HRS} values of **2NMe₂** and **3NO₂** measured at 1064 nm, which are equal to 19100 and 8500 a.u., respectively.

Table 6: β_{HRS} (a.u.) and DR values obtained from HRS measurements in chloroform using incident wavelengths of 1064 and 1300 nm.

	1064 nm		**1300 nm**	
	β_{HRS}	DR	β_{HRS}	DR
1NMe₂	14000 ± 1000	5.1 ± 0.5	5600 ± 300	5.2 ± 0.9
2NMe₂	19100 ± 1400	5.7 ± 0.4	7400 ± 200	4.5 ± 0.3
3NMe₂	8500 ± 400	4.9 ± 0.5	ND	
3H	PS		ND	
3NHAc	ND		ND	
3NO₂	8600 ± 400	5.1 ± 0.8	ND	
4H	11700 ± 500	4.9 ± 0.4	ND	
4NO₂	TPA		17600 ± 500	5.0 ± 0.2
5H	5000 ± 200	5.6 ± 0.5	3600 ± 300	3.3 ± 0.4
L1-4NO₂	TPA		19100 ± 2000	4.84 ± 0.07

L2-4NO$_2$	TPA	22000 ± 1500	4.82 ± 0.08

PS: Photoswitching observed during the HRS measurements, permanently decreasing the HRS signal.
ND: HRS signal below the detection limit.
TPA: Two-photon absorption, strongly perturbed HRS signal.

Compounds incorporating one donor (D-π type, such as **3H**, **5H** and **4H**), two weak donors with similar strengths (d-π-d type such as **3NHAc**) or two donors with different strengths (d-π-D type, such as **3NMe$_2$** and **1NMe$_2$**), give rise to weaker β_{HRS} responses. The NLO responses of d-π-d and d-π-D compounds measured at 1064 nm partly originate from frequency dispersion effects, the strongest hyperpolarizabilities being associated to the largest maximum absorption wavelengths. At 1300 nm, only **1NMe$_2$** has a non-negligible β_{HRS} response. **3NHAc** has the weakest response that we could not even measure at 1064 nm. Among the D-π compounds, **4H** exhibits the strongest β_{HRS} at 1064 nm with 11700 a.u., while only **5H** could be still measured at 1300 nm. Note that the β_{HRS} at 1064 nm could not be determined for **3H**, as we observed a constant decrease of the HRS signal with time. We interpret this behavior as follows: the absorption band of **3H** occurs at 343 nm (see Table 2), which is very close to the third harmonic scattering (THS) of the solution, which occurs at 1064/3 = 354.67 nm. Under these conditions, we believe that THS photoactivates the *trans* to *cis* isomerization. Note that THS is symmetry-allowed and more efficient in solution than the second harmonic scattering (HRS).[54] Obviously, we may expect that this photoisomerization due to THS occurs also with **3NHAc** whose absorption maximum lies at 359 nm (Table 2). However, we could not observe such behavior, probably because the HRS response of **3NHAc** was too weak at 1064 nm.

The computed NLO properties of *trans* and *cis* compounds are reported in Table 7 and Figure 6a. Figure 7 shows that the calculated β_{HRS} values for *trans* isomers correlate well with the experimental ones. Moreover, DFT calculations predict that the β_{HRS} responses decrease upon *trans-cis* photoisomerization ~~owing to the loss of π-electron conjugation~~. Apart for **3NHAc** whose *trans* form has a near centrosymmetric electronic structure (of quadrupolar nature), the computed NLO contrasts (Figure 6b) range between 2 and 5 for all compounds, regardless of the incident wavelength. The largest contrasts are obtained for push-pull derivatives **2NMe$_2$**, **3NO$_2$** and **4NO$_2$**.

Table 7: β_{HRS} (10^2 a.u.) and DR values calculated at the TDDFT/M06-2X/6-311+G(d) level in chloroform using incident wavelengths of 1064 nm, 1300 nm and in the static limit[(1)] for *trans* and *cis* isomers.

	Trans						***Cis***					
	1064 nm		**1300 nm**		**static**		**1064 nm**		**1300 nm**		**Static**	
	β_{HRS}	DR	β_{HRS}	DR	β_{HRS}	DR	β_{HRS}	DR	β_{HRS}	DR	β_{HRS}	DR
0H	0	-	0	-	0	-	2	2.72	2	2.66	1	2.58
1NMe$_2$	106	4.93	70	4.89	38	4.80	46	4.22	27	4.39	17	4.27
2NMe$_2$	190	4.89	126	4.83	69	4.71	58	4.91	35	5.20	21	5.25
3NMe$_2$	85	4.89	57	4.83	31	4.71	42	4.21	26	4.24	16	4.07
3H	25	4.89	20	4.88	13	4.85	11	4.45	8	4.56	6	4.57
3NHAc	2	4.47	2	4.53	2	4.49	13	3.40	9	3.47	6	3.43
3NO$_2$	103	4.88	76	4.82	46	4.72	31	4.99	19	5.77	12	5.92
4H	110	4.91	77	4.87	45	4.79	41	4.67	27	4.71	17	4.60
4NO$_2$	400	4.96	240	4.91	118	4.80	96	4.90	51	5.65	28	5.85
5H	82	4.87	59	4.82	35	4.72	34	4.61	23	4.65	14	4.53
L1-4NO$_2$	417	4.97	249	4.93	152	4.83	94	4.93	50	5.72	35	5.93
L2-4NO$_2$	416	4.97	248	4.92	151	4.82	93	4.91	49	5.69	34	5.89

(1) Calculated using the optical dielectric constant of chloroform, $\epsilon_\infty = 2.09$. See Tables S14-S15 and Figure S14 the comparison with static first hyperpolarizabilities computed using ϵ_0.

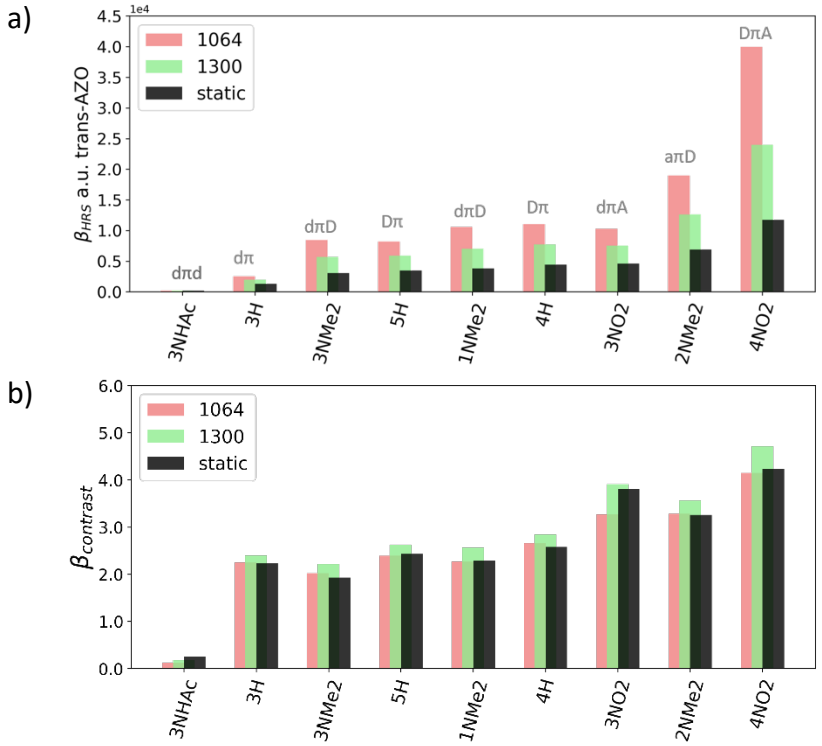

Figure 6: (a) Dynamic and static β_{HRS} responses (in 10^4 a.u.) of *trans* isomers computed at the TDDFT/M06-2X/6-311+G(d) level in chloroform, with the substitution pattern of the

compounds (a/A and d/D stand for weak/strong acceptors and donors, respectively). (b) trans/cis β_{HRS} contrasts.

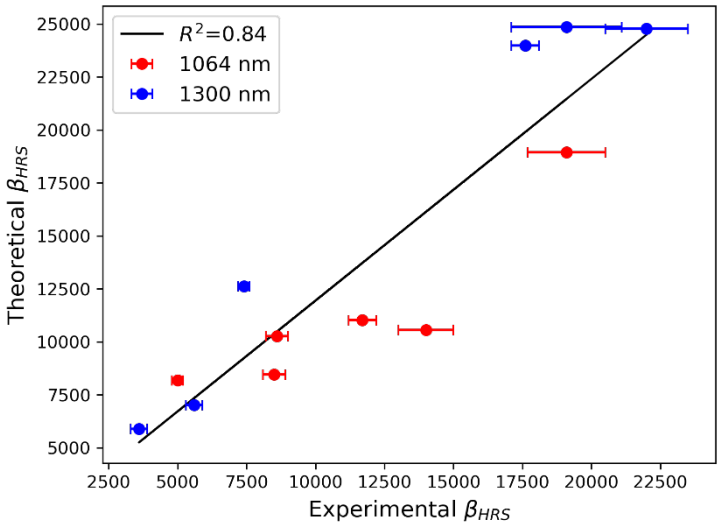

Figure 7: Correlation between experimental and computed β_{HRS} values at 1064 nm (red) and 1300 nm (blue).

Both experimental and calculated depolarization ratios for *trans* isomers are close to 5, revealing a 1D symmetry of the NLO responses. A significant decrease of the measured DR upon changing the laser excitation to lower energy is observed for **5H** and (to a lesser extent) **2NMe$_2$**, but this variation is not reproduced by DFT calculations, which do not evidence sizeable frequency resonance effects on DR. All computed DR are very similar and lie in the small 4.8-4.9 range, again with the exception of **3NHAc** for which DR is smaller (4.5). A much higher dispersion is found in the DR values of the *cis* forms, which vary from 3.47 (**3NHAc**) to 5.77 (**3NO$_2$**) at 1300 nm. In addition, while all compounds except **3NHAc** show a decrease in β_{HRS} upon *trans-cis* photoisomerization, the variation of DR depends on the donor-acceptor substitution pattern: it increases for the strongest push-pull derivatives **2NMe$_2$**, **3NO$_2$** and **4NO$_2$**, and decreases for all other compounds. According to equation 4, the concomitant β_{HRS} lowering and DR enhancement found for push-pull systems is due to a larger decrease of the $\langle\beta^2_{ZXX}\rangle$ component. The change in the symmetry of the NLO response upon photoisomerization is further illustrated in Figure 8 for representative compounds using the unit sphere representation (USR) of the first hyperpolarizability tensor.

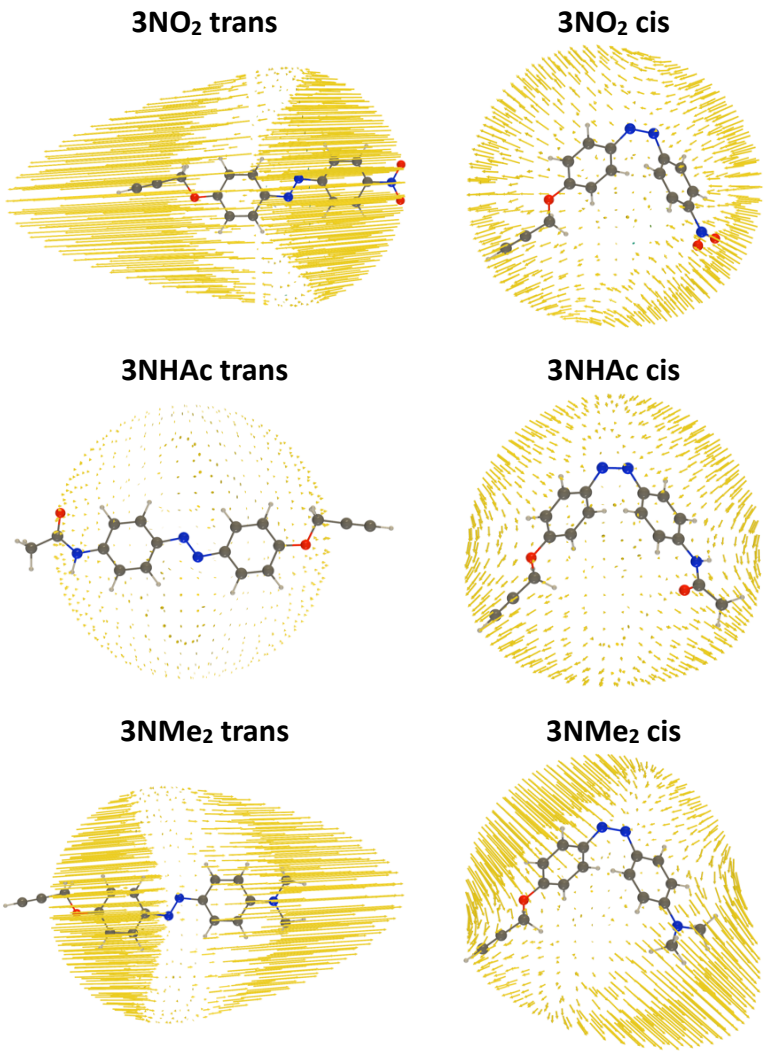

Figure 8: Unit sphere representation of the first hyperpolarizability tensor of representative compounds in their *trans* (left) and *cis* (right) forms, as calculated at the TDDFT/M06-2X/6-311+G(d) level in chloroform using an incident wavelength of 1300 nm.

3.4.2 *Analyses using the two-state approximation*

To further rationalize the relative magnitude of the quadratic NLO responses of *trans* isomers, we rely in this section on the two-state approximation (TSA). First introduced by Oudar and Chemla,[55] this approximation truncates the sum-over-state (SOS) expansion of the β tensor components to the only contribution of the lowest-energy dipole-allowed electronic excited state (here S_2). In that case, after assuming a single non-negligible diagonal β tensor component, β_{HRS} can be simply expressed in terms of the spectroscopic data (transition energies, oscillator strengths and dipole moment variations) collected in Tables 3 and 4:

$$\beta_{HRS}^{TSA} = 9\sqrt{\frac{6}{35}}\frac{f_{02}\Delta\mu_{02}}{\Delta E_{02}^3}F(\omega) \qquad (5)$$

$F(\omega)$ is a factor accounting for frequency dispersion, which depends on the energy $\hbar\omega$ of the incident photons:

$$F(\omega) = \frac{\Delta E_{02}^4}{(\Delta E_{02}^2 - (\hbar\omega)^2)(\Delta E_{02}^2 - (2\hbar\omega)^2)} \qquad (6)$$

The excellent correlation existing between the β_{HRS} responses calculated at the TDDFT level and those estimated using the TSA (Figure 9a and Table S16, SI3) demonstrates that the relative magnitude of the hyperpolarizability in this series of derivatives is fully determined by the $S_0 \rightarrow S_2$ transition. Thus, the high second-order β_{HRS} calculated for **4NO$_2$** (and to a lesser extent for **2NMe$_2$** and **3NO$_2$**) can be attributed to smaller excitation energies and larger oscillator strengths (Table 3), as well as much larger dipole moment variations of the $S_0 \rightarrow S_2$ transition. The latter find their origin in the larger extent of the photoinduced intramolecular charge transfer (Table 4). Furthermore, the resonance enhancement factors, estimated as the ratio between dynamic and static β_{HRS} values computed at the TDDFT level, are compared in Figure 9b to the 2-state dispersion factor (equation 6). The plot clearly indicates that, although the TSA provides slightly underestimated $F(\omega)$ values, it reproduces well the TDDFT data in this low resonance regime.

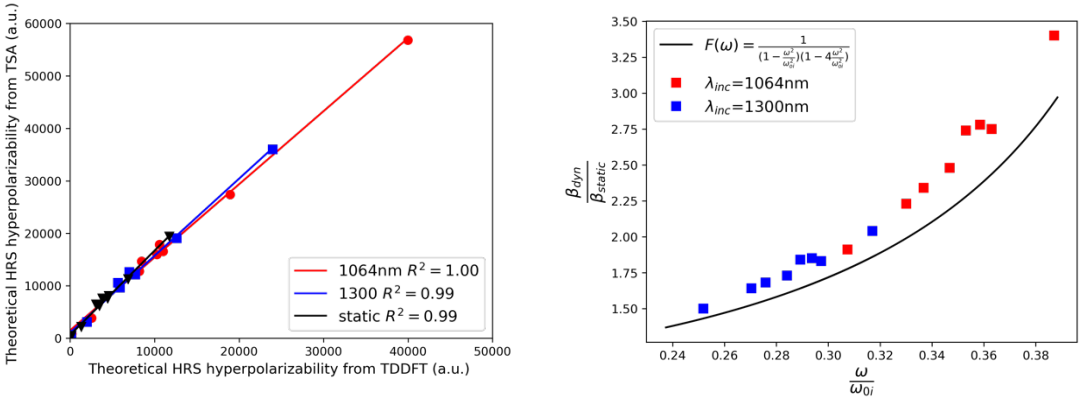

(a) (b)

Figure 9: (a) correlation between β_{HRS}^{TSA} and β_{HRS}^{TDDFT} values for *trans* isomers. (b) Frequency dispersion enhancement on the HRS hyperpolarizabilities of *trans* isomers. The black line represents the frequency dispersion factor evaluated using the 2-state approximation (Equation 6). The color points represent the frequency dispersion evaluated using TDDFT, as the ratio between the dynamic and static responses (using the optical dielectric constant of chloroform in the IEF-PCM scheme). The $F(\omega)$ values computed for **3NHAc** have been excluded from the plot, owing to its negligible NLO response.

3.5 Effect of the anchoring unit

In the last part of this study, we addressed the impact of clicking a triazole bearing long carbon chain (11 carbons) on the alkyne on the linear and nonlinear optical properties of *trans* azobenzenes, as this strategy is used in surface chemistry to electronically decouple the photochromic units from the substrate. **4NO₂** was selected as representative of compounds with strong push-pull character that are able to deliver strong SHG signal. Two additional derivatives, **L1-4NO₂** and **L2-4NO₂**, were thus prepared by means of copper-catalized Huisgen 1,3-cycloaddition with corresponding azide chains (Figure 10).

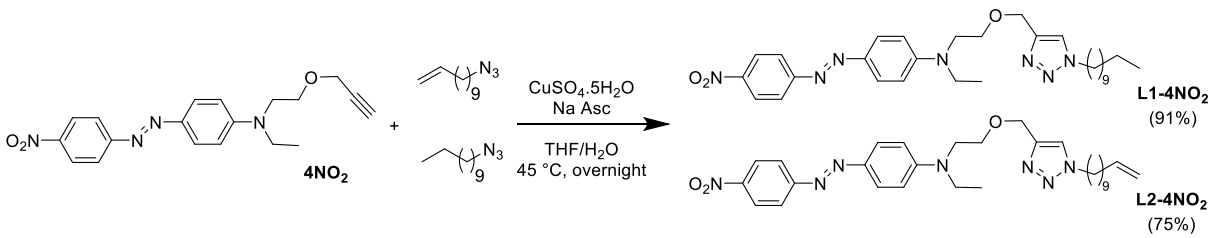

Figure 10: Synthesis of **L1-4NO₂** and **L2-4NO₂** by Huisgen click reaction between azide chains and **4NO₂**.

As shown in Table 2 and Figure 11, **L1-4NO₂** and **L2-4NO₂** display absorption spectra very similar to **4NO₂**, evidencing the negligible impact of the anchoring chain. This result is consistent with DFT simulations (Figure S16) and results from the lack of delocalization of the MOs involved in the main transitions over the anchoring chain (Figure S15). The impact on the NLO response is slightly more pronounced, with an increase of 9% (**L1-4NO₂**) and 25% (**L2-4NO₂**) of the HRS hyperpolarizability with respect to **4NO₂** (Table 6). However, owing to the experimental uncertainties, the NLO response of **L1-4NO₂** and **L2-4NO₂** can be considered as similar. The enhancement of the NLO response upon the triazole addition might be related to the increase in the permanent dipole moment (9.7 D for **4NO₂** vs ~14 D for **L1-4NO₂** and **L2-4NO₂**, see Table 1), which is expected to induce larger polarization interactions with the solvent molecules. The increase of β_{HRS} is partially reproduced by DFT calculations using the IEF-PCM continuum solvent model, although its amplitude is underestimated (Table 7). Overall, we can conclude from these results that the addition of the triazole unit does not change the absorption and slightly enhances the second-order nonlinear optical response of the photochromic units, which is beneficial for further applications.

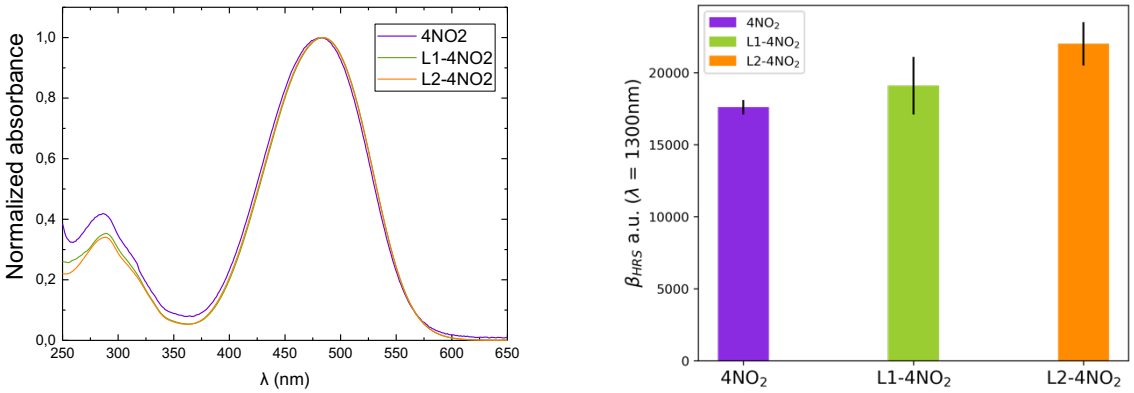

(a) (b)

Figure 11: (a) Absorption spectra and (b) β_{HRS} responses (in 10^4 a.u.) of *trans* **4NO₂**, **L1-4NO₂** and **L2-4NO₂** measured in chloroform solutions.

4 Conclusion

In this study presents an in-depth investigation of the photophysical properties of clickable azobenzene derivatives, including their photoswitching and second-order nonlinear optical properties. Selecting the appropriate excitation and probe wavelengths allowed to trigger and monitor the *trans-cis* photoswitching of the compounds, revealing different behaviors depending on their chemical functionalization. In particular, fast and efficient *trans-cis* photoswitching with slow thermal back reaction was recorded for **4H** and for derivatives bearing a dimethylamino donor group (**1NMe₂**, **2NMe₂**, **3NMe₂**) upon irradiation at 405 nm and probe at 420 nm. Hyper-Rayleigh Scattering measurements combined to DFT calculations also allowed to investigate the impact of chemical substitution on the magnitude and dipolar/octopolar nature of the second-harmonic signal, as well as on the NLO contrast upon photoisomerization. The results show that the magnitude of the SHG signal can be finely tuned by appropriate chemical design, the largest responses and contrasts being expectedly obtained when strong donor and acceptor groups are linked at the opposite extremities of the azobenzene core. Among the investigated compounds, **4NO₂** indeed provides the largest NLO responses and *trans*/*cis* β_{HRS} contrast thanks to its push-pull architecture favoring photoinduced intramolecular charge transfer. However, this derivative displays a low photoswitching rate. On the other hand, **2NMe₂** combines a fast kinetics behavior in both the forward and backward isomerization reactions, together with a large (although smaller than **4NO₂**) NLO response in its *trans* form and a large β contrast. In conclusion, this study shows how highly dipolar structures are promising for second harmonic responses in solution.

However, their integration in light-sensitive 2D NLO devices may not be the best compromise, as electrostatic dipole-dipole interactions are expected to hinder the parallel ordering of molecular units after anchoring on a solid substrate. For this reason, the collection of azobenzene derivatives proposed in this work has been designed to provide a large range of NLO responses and dipole magnitude, offering different balances for further integration into self-assembled monolayers.

Acknowledgement

This work was supported by the French National Research Agency (grant number ANR-20-CE29-0009-01). V.R. thanks the Région Nouvelle Aquitaine for financial support (CRA: 2015-1R10205-00004858). V.R. is grateful to F. Adamietz for experimental support and technical developments. The authors also acknowledge financial support from the IdEx University of Bordeaux / Grand Research Program "GPR LIGHT" (convention OPE-2021-0316). Calculations were performed using the computing facilities provided by the "Mésocentre de Calcul Intensif Aquitain" (MCIA) of the University of Bordeaux and of the Université de Pau et des Pays de l'Adour.

Supporting Information Available

Part 1 (SI1): Organic synthesis: NMR, IR and mass spectra of all investigated derivatives (PDF).

Part 2 (SI2): Spectroscopy characterizations: HRS measurements and photoswitching kinetics (PDF).

Part 3 (SI3): Computational results: selection of the level of approximation for geometry optimization, structural and electronic properties of trans and cis forms, absorption and NLO properties (PDF).

References

[1] Binder WH, Sachsenhofer R. 'Click' Chemistry in Polymer and Materials Science. Macromol Rapid Commun 2007;28:15–54. https://doi.org/https://doi.org/10.1002/marc.200600625.

[2] Nebhani L, Barner-Kowollik C. Orthogonal Transformations on Solid Substrates: Efficient Avenues to Surface Modification. Advanced Materials 2009;21:3442–68. https://doi.org/https://doi.org/10.1002/adma.200900238.

[3] Wendeln C, Ravoo BJ. Surface Patterning by Microcontact Chemistry. Langmuir 2012;28:5527–38. https://doi.org/10.1021/la204721x.

[4] Al-Hajj N, Mousli Y, Miche A, Humblot V, Hunel J, Heuzé K, et al. Influence of the grafting process on the orientation and the reactivity of azide-terminated monolayers onto silica surface. Appl Surf Sci 2020;527:146778. https://doi.org/https://doi.org/10.1016/j.apsusc.2020.146778.
[5] Yaakov N, Chaikin Y, Wexselblatt E, Tor Y, Vaskevich A, Rubinstein I. Application of Surface Click Reactions to Localized Surface Plasmon Resonance (LSPR) Biosensing. Chemistry – A European Journal 2017;23:10148–55. https://doi.org/https://doi.org/10.1002/chem.201701511.
[6] Mendes PM. Stimuli-responsive surfaces for bio-applications. Chem Soc Rev 2008;37:2512–29. https://doi.org/10.1039/B714635N.
[7] Zhang J, Ma W, He XP, Tian H. Taking Orders from Light: Photo-Switchable Working/Inactive Smart Surfaces for Protein and Cell Adhesion. ACS Appl Mater Interfaces 2017;9:8498–507. https://doi.org/10.1021/acsami.6b15599.
[8] Castet F, Rodriguez V, Pozzo J-L, Ducasse L, Plaquet A, Champagne B. Design and characterization of molecular nonlinear optical switches. Acc Chem Res 2013;46. https://doi.org/10.1021/ar4000955.
[9] Coe BJ. Nonlinear Optical Properties Responses in Molecular Materials. Chem Eur J 1999;5:2464–71.
[10] Plaquet A, Guillaume M, Champagne B, Castet F, Ducasse L, Pozzo J-L, et al. In silico optimization of merocyanine-spiropyran compounds as second-order nonlinear optical molecular switches. Physical Chemistry Chemical Physics 2008;10. https://doi.org/10.1039/b806561f.
[11] Beaujean P, Bondu F, Plaquet A, Garcia-Amorós J, Cusido J, Raymo FM, et al. Oxazines: A New Class of Second-Order Nonlinear Optical Switches. J Am Chem Soc 2016;138. https://doi.org/10.1021/jacs.5b13243.
[12] Tonnelé C, Castet F. Nonlinear optical properties of spirocyclohexadine photochromes: Insights from DFT calculations. Photochemical and Photobiological Sciences 2019;18:2759–65. https://doi.org/10.1039/c9pp00312f.
[13] Pielak K, Bondu F, Sanguinet L, Rodriguez V, Champagne B, Castet F. Second-order nonlinear optical properties of multiaddressable indolinooxazolidine derivatives: Joint Computational and hyper-Rayleigh scattering investigations. Journal of Physical Chemistry C 2017;121. https://doi.org/10.1021/acs.jpcc.6b11082.
[14] Pielak K, Bondu F, Sanguinet L, Rodriguez V, Castet F, Champagne B. Acido-triggered switching of the second-order nonlinear optical properties of a ferrocenyl-containing indolino-oxazolidine derivative. Dyes and Pigments 2019;160. https://doi.org/10.1016/j.dyepig.2018.07.007.
[15] Quertinmont J, Beaujean P, Stiennon J, Aidibi Y, Leriche P, Rodriguez V, et al. Combining Benzazolo-Oxazolidine Twins toward Multi-state Nonlinear Optical Switches. J Phys Chem B 2021;125:3918–31. https://doi.org/10.1021/acs.jpcb.1c01962.
[16] Pielak K, Tonnelé C, Sanguinet L, Cariati E, Righetto S, Muccioli L, et al. Dynamical Behavior and Second Harmonic Generation Responses in Acido-Triggered Molecular Switches. Journal of Physical Chemistry C 2018;122. https://doi.org/10.1021/acs.jpcc.8b08697.
[17] Sanguinet L, Pozzo J-L, Rodriguez V, Adamietz F, Castet F, Ducasse L, et al. Acido- And phototriggered NLO properties enhancement. Journal of Physical Chemistry B 2005;109. https://doi.org/10.1021/jp0442450.

[18] Mançois F, Sanguinet L, Pozzo J-L, Guillaume M, Champagne B, Rodriguez V, et al. Acido-triggered nonlinear optical switches: Benzazolo-oxazolidines. Journal of Physical Chemistry B 2007;111. https://doi.org/10.1021/jp073386.
[19] Sanguinet L, Pozzo J-L, Guillaume M, Champagne B, Castet F, Ducasse L, et al. Acidoswitchable NLO-phores; Benzimidazolo[2,3-b]oxazolidines. Journal of Physical Chemistry B 2006;110. https://doi.org/10.1021/jp060825g.
[20] Giraud M, Léaustic A, Guillot R, Yu P, Lacroix PG, Nakatani K, et al. Dithiazolylethene-based molecular switches for nonlinear optical properties and fluorescence: synthesis, crystal structure and ligating properties. J Mater Chem 2007;17:4414–25. https://doi.org/10.1039/B704806H.
[21] Gilat SL, Kawai SH, Lehn J-M. Light-Triggered Molecular Devices: Photochemical Switching Of optical and Electrochemical Properties in Molecular Wire Type Diarylethene Species. Chemistry – A European Journal 1995;1:275–84. https://doi.org/https://doi.org/10.1002/chem.19950010504.
[22] Plaquet A, Champagne B, Castet F, Ducasse L, Bogdan E, Rodriguez V, et al. Theoretical investigation of the dynamic first hyperpolarizability of DHA-VHF molecular switches. New Journal of Chemistry 2009;33:1349–56. https://doi.org/10.1039/b900432g.
[23] Schulze M, Utecht M, Hebert A, Rück-Braun K, Saalfrank P, Tegeder P. Reversible photoswitching of the interfacial nonlinear optical response. Journal of Physical Chemistry Letters 2015;6:505–9. https://doi.org/10.1021/jz502477m.
[24] Hänsel M, Barta C, Rietze C, Utecht M, Rück-Braun K, Saalfrank P, et al. Two-Dimensional Nonlinear Optical Switching Materials: Molecular Engineering toward High Nonlinear Optical Contrasts. The Journal of Physical Chemistry C 2018;122:25555–64. https://doi.org/10.1021/acs.jpcc.8b08212.
[25] Tonnelé C, Champagne B, Muccioli L, Castet F. Second-order nonlinear optical properties of Stenhouse photoswitches: Insights from density functional theory. Physical Chemistry Chemical Physics 2018;20:27658–67. https://doi.org/10.1039/c8cp05843a.
[26] Dubuis S, Dellai A, Courdurié C, Owona J, Kalafatis A, Vellutini L, et al. Nonlinear Optical Responses of Photoswitchable Donor–Acceptor Stenhouse Adducts. J Am Chem Soc 2023;145:10861–71. https://doi.org/10.1021/jacs.3c02778.
[27] Plaquet A, Guillaume M, Champagne B, Rougier L, Mançois F, Rodriguez V, et al. Investigation on the second-order nonlinear optical responses in the keto-enol equilibrium of anil derivatives. Journal of Physical Chemistry C 2008;112. https://doi.org/10.1021/jp711511t.
[28] Ségerie A, Castet F, Kanoun MB, Plaquet A, Liégeois V, Champagne B. Nonlinear optical switching behavior in the solid state: A theoretical investigation on anils. Chemistry of Materials 2011;23. https://doi.org/10.1021/cm2015516.
[29] Sliwa M, Létard S, Malfant I, Nierlich M, Lacroix PG, Asahi T, et al. Design, Synthesis, Structural and Nonlinear Optical Properties of Photochromic Crystals: Toward Reversible Molecular Switches. Chemistry of Materials 2005;17:4727–35. https://doi.org/10.1021/cm050929o.
[30] Asahi T, Masuhara H, Nakatani K, Sliwa M. Photochromic Dynamics of Salicylidene Aniline in Solid State by Using Femtosecond Transient Absorption Spectroscopy. Molecular Crystals and Liquid Crystals 2005;431:541–8. https://doi.org/10.1080/15421400590947351.

[31] Nakatani K, Delaire JA. Reversible Photoswitching of Second-Order Nonlinear Optical Properties in an Organic Photochromic Crystal. Chemistry of Materials 1997;9:2682–4. https://doi.org/10.1021/cm970369w.
[32] Lucas LN, Jong JJD de, Esch JH van, Kellogg RM, Feringa BL. Syntheses of Dithienylcyclopentene Optical Molecular Switches. European J Org Chem 2003;2003:155–66. https://doi.org/https://doi.org/10.1002/1099-0690(200301)2003:1<155::AID-EJOC155>3.0.CO;2-S.
[33] Hadjoudis E, Mavridis I. Photochromism and Thermochromism of Schiff Bases in the Solid State: Structural Aspects. Chem Soc Rev 2004;33:579–88. https://doi.org/10.1039/b303644h.
[34] Loucif-Saibi R, Nakatani K, Delaire JA, Dumont M, Sekkat Z. Photoisomerization and second harmonic generation in disperse red one-doped and -functionalized poly(methyl methacrylate) films. Chemistry of Materials 1993;5:229–36. https://doi.org/10.1021/cm00026a014.
[35] Schulze M, Utecht M, Moldt T, Przyrembel D, Gahl C, Weinelt M, et al. Nonlinear optical response of photochromic azobenzene-functionalized self-assembled monolayers. Physical Chemistry Chemical Physics 2015;17:18079–86. https://doi.org/10.1039/c5cp03093e.
[36] Tonnelé C, Champagne B, Muccioli L, Castet F. Nonlinear Optical Contrast in Azobenzene-Based Self-Assembled Monolayers. Chemistry of Materials 2019;31:6759–69. https://doi.org/10.1021/acs.chemmater.9b01241.
[37] Asif MF, Bano R, Farooq R, Muhammad S, Mahmood T, Ayub K, et al. Shedding light on the second order nonlinear optical responses of commercially available acidic azo dyes for laser applications. Dyes and Pigments 2022;202:110284. https://doi.org/https://doi.org/10.1016/j.dyepig.2022.110284.
[38] Pimenta ÂCM, Andrade-Filho T, Manzoni V, Del Nero J, Gester R. Giant values obtained for first hyperpolarizabilities of methyl orange: a DFT investigation. Theor Chem Acc 2019;138:27. https://doi.org/10.1007/s00214-018-2406-x.
[39] Jaunet-Lahary T, Chantzis A, Chen KJ, Laurent AD, Jacquemin D. Designing Efficient Azobenzene and Azothiophene Nonlinear Optical Photochromes. The Journal of Physical Chemistry C 2014;118:28831–41. https://doi.org/10.1021/jp510581m.
[40] Kleinpeter E, Bölke U, Kreicberga J. Quantification of the push-pull character of azo dyes and a basis for their evaluation as potential nonlinear optical materials. Tetrahedron 2010;66:4503–9. https://doi.org/10.1016/j.tet.2010.04.067.
[41] Reis H. Problems in the comparison of theoretical and experimental hyperpolarizabilities revisited. J Chem Phys 2006;125:014506. https://doi.org/10.1063/1.2211611.
[42] Chai J Da, Head-Gordon M. Long-range corrected hybrid density functionals with damped atom-atom dispersion corrections. Physical Chemistry Chemical Physics 2008;10:6615–20. https://doi.org/10.1039/b810189b.
[43] Naim C, Castet F, Matito E. Impact of van der Waals interactions on the structural and nonlinear optical properties of azobenzene switches. Physical Chemistry Chemical Physics 2021;23:21227–39. https://doi.org/10.1039/d1cp02500g.
[44] Schweighauser L, Strauss MA, Bellotto S, Wegner HA. Attraction or Repulsion? London Dispersion Forces Control Azobenzene Switches. Angewandte Chemie International Edition 2015;54:13436–9. https://doi.org/https://doi.org/10.1002/anie.201506126.

[45] Zhao Y, Truhlar DG. The M06 suite of density functionals for main group thermochemistry, thermochemical kinetics, noncovalent interactions, excited states, and transition elements: Two new functionals and systematic testing of four M06-class functionals and 12 other function. Theor Chem Acc 2008;120:215–41. https://doi.org/10.1007/s00214-007-0310-x.
[46] Lescos L, Sitkiewicz SP, Beaujean P, Blanchard-Desce M, Champagne B, Matito E, et al. Performance of DFT functionals for calculating the second-order nonlinear optical properties of dipolar merocyanines. Physical Chemistry Chemical Physics 2020;22:16579–94. https://doi.org/10.1039/d0cp02992k.
[47] Johnson LE, Dalton LR, Robinson BH. Optimizing Calculations of Electronic Excitations and Relative Hyperpolarizabilities of Electrooptic Chromophores. Acc Chem Res 2014;47:3258–65. https://doi.org/10.1021/ar5000727.
[48] Tomasi J, Mennucci B, Cammi R. Quantum mechanical continuum solvation models. Chem Rev 2005;105:2999–3093. https://doi.org/10.1021/cr9904009.
[49] Vetráková Ľ, Ladányi V, Al Anshori J, Dvořák P, Wirz J, Heger D. The absorption spectrum of: Cis -azobenzene. Photochemical and Photobiological Sciences 2017;16:1749–56. https://doi.org/10.1039/c7pp00314e.
[50] Le Bahers T, Adamo C, Ciofini I. A qualitative index of spatial extent in charge-transfer excitations. J Chem Theory Comput 2011;7:2498–506. https://doi.org/10.1021/ct200308m.
[51] Jacquemin D, Le Bahers T, Adamo C, Ciofini I. What is the “best” atomic charge model to describe through-space charge-transfer excitations? Physical Chemistry Chemical Physics 2012;14:5383–8. https://doi.org/10.1039/c2cp40261k.
[52] García-Amorós J, Velasco D. Recent advances towards azobenzene-based light-driven real-time information-transmitting materials. Beilstein Journal of Organic Chemistry 2012;8:1003–17. https://doi.org/10.3762/bjoc.8.113.
[53] Bandara HMD, Burdette SC. Photoisomerization in different classes of azobenzene. Chem Soc Rev 2012;41:1809–25. https://doi.org/10.1039/C1CS15179G.
[54] Rodriguez V. Polarization-Resolved Third-Harmonic Scattering in Liquids. The Journal of Physical Chemistry C 2017;121:8510–4. https://doi.org/10.1021/acs.jpcc.7b00983.
[55] Oudar JL, Chemla DS. Hyperpolarizabilities of the nitroanilines and their relations to the excited state dipole moment. J Chem Phys 1976;66:2664–8. https://doi.org/10.1063/1.434213.